



Article

Development of a Vertical Submerging and Emerging Bat-Ray-Inspired Underwater Vehicle

Enrique Mar-Castro , Sergio Alejandro May-Rodríguez , Rafael Stanley Núñez-Cruz * ,
Elba Dolores Antonio-Yañez , Luis Mario Aparicio-Lastiri and Juan Herrera-Vidal

Control and Design Laboratory, Polytechnic University of Tulancingo, Tulancingo de Bravo 43629, Mexico; enrique.mar2415005@upt.edu.mx (E.M.-C.); sergio.alejandror2231092@upt.edu.mx (S.A.M.-R.); elba.antonio@upt.edu.mx (E.D.A.-Y.); luis.aparicio2415004@upt.edu.mx (L.M.A.-L.); juan.herrera2315007@upt.edu.mx (J.H.-V.)

* Correspondence: rafael.nunez@upt.edu.mx

Abstract: In this article, the development of a bat-ray-inspired underwater vehicle is presented; although the propulsion of the vehicle is based on traditional thrusters, the shape of the ray's fins was used as a model to design the body of the vehicle; this architecture allows the independent control of the forward velocity and the full attitude of the vehicle using only two thrusters and two articulated fins. The compact design of the robot, along with the high dexterity of the architecture, allows the vehicle to submerge and emerge vertically as well as navigate horizontally. The mathematical model of the proposed vehicle, including dynamics and propulsion system, is presented and validated using numerical simulations. Finally, experimental tests are presented to demonstrate the capabilities of the proposed design.

Keywords: bio-inspired design; remote-operated vehicle; mathematical modeling of underwater robots; vertical submerging and emerging underwater vehicles



Citation: Mar-Castro, E.; May-Rodríguez, S.A.; Núñez-Cruz, R.S.; Antonio-Yañez, E.D.; Aparicio-Lastiri, L.M.; Herrera-Vidal, J. Development of a Vertical Submerging and Emerging Bat-Ray-Inspired Underwater Vehicle. *Biomimetics* **2024**, *9*, 582. <https://doi.org/10.3390/biomimetics9100582>

Academic Editor: Shunichi Kobayashi

Received: 25 August 2024

Revised: 19 September 2024

Accepted: 22 September 2024

Published: 25 September 2024



Copyright: © 2024 by the authors. Licensee MDPI, Basel, Switzerland. This article is an open access article distributed under the terms and conditions of the Creative Commons Attribution (CC BY) license (<https://creativecommons.org/licenses/by/4.0/>).

1. Introduction

Across the vast expanse of the oceans, researchers and engineers have been inspired by the complex designs and amazing abilities of nature's aquatic inhabitants, creating a new generation of bio-inspired underwater vehicles. Bio-inspired machines seek to achieve the unique capabilities that allow aquatic animals to move efficiently, live under high atmospheric pressures, and conserve energy via mimicking the morphology, behavior, and locomotion of these organisms.

Biomimetics of marine animals has been applied to the design of sensors, locomotion mechanisms, and to define the shape of robot bodies. Some applications of bio-inspired sensors are the measurement of the velocity of fluid surrounding a robot [1], detection of disturbances in fluids [2], and emulating touch and obtaining information about objects grabbed by a manipulator [3], among others.

Locomotion inspired by marine animals focuses on replicating the efficient movement mechanisms and swimming patterns of creatures such as fish, cephalopods, and aquatic mammals by using fins, tails, and flexible structures. According to Sun et al. [4], there are two basic forms of locomotion: the first is known as body and caudal fin (BCF), in this type of swimming the body is bent in a wave-backward propulsion that extends to the tail fin. The second form of basic locomotion is the so-called median and paired fin (MCF), in which the swimmer uses these elements to gain propulsion. Currently, different robots have been developed that imitate these types of locomotion; for example, fish-based robots [5,6] can use a system of pectoral and caudal fins to maneuver in small spaces and perform rapid turns, while those inspired by cephalopods [7] can take advantage of jet propulsion to achieve fast and precise movements.

The morphology of aquatic animals provides them with characteristics and hydrodynamic capabilities that are of great interest for the development of new robotic prototypes. For example, robots that emulate sea snakes [8,9] use flexible, segmented bodies to move nimbly in complex underwater environments, replicating their undulating movements. Jellyfish [10,11], with their jet propulsion system based on the contraction and expansion of their bell, have inspired the design of robots that can navigate smoothly and with energy consumption reduced. Turtles [12,13], with their ability to navigate long distances and their efficient hydrodynamic profile, are also being studied to improve the navigability and efficiency of underwater robots in long-distance explorations and in diverse marine environments. Finally, the rays [14–16], with their undulating flapping motion, have served as a model for developing robotic fins that provide superior maneuverability in underwater robots, in addition to their structure providing greater stability.

To select the marine animal intended for mimicry, it is necessary to carry out an analysis of the project's needs. Some variables to consider are maneuverability, flexibility, hydrodynamics, speed, and stability of the platform. In this work, a platform is sought that has high maneuverability and good hydrodynamic characteristics, which allow inspection and marine archaeology tasks to be carried out. With this in mind, and having made a comparison of the different existing structures, the one based on a ray was selected. These animals have high maneuverability and stability; however, their movement is slow and inefficient and replicating the movement of the fins is a very complicated task due to the large number of muscles that these animals possess. For this reason, the maneuverability that many of these prototypes have is classified between low and medium.

The aim of this project was to develop a novel unmanned underwater vehicle which is stable, fast, maneuverable, able to navigate efficiently, but also capable of hovering over a specific area for inspection or mapping applications. To accomplish this goal, the authors propose a novel design which, although it is actuated using traditional thrusters, is able to exhibit high moving efficiency because the shape of the body is inspired by the shape of the ray's fins, which are articulated to produce changes in the direction of movement.

Figure 1 shows the exterior design of the proposed vehicle, although there are benefits in trying to fully mimic the shape and locomotion of bat rays, the resulting designs are usually bulky and not sufficiently agile [17]. On the other hand, traditional propulsion technologies are well developed and easy to control for high-speed underwater locomotion. In the proposed design, the downside of using thrusters as the propulsion system is compensated by the hydrodynamics of the ray's shape to produce a design with high maneuverability, agility, and efficiency characteristics.

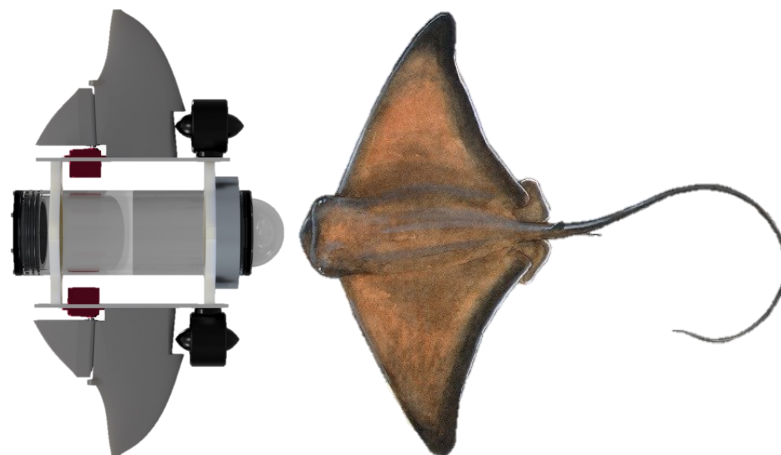


Figure 1. On the left side is the proposed vehicle, on the right side a photo of a bat ray; extracted from the “Marine Species Portal” at <https://marinespecies.wildlife.ca.gov/bat-ray/>, accessed on 19 August 2024.

2. Bio-Inspired Robot Design

The design of an underwater robot involves many important choices, for example, the type of shape, hull, and locomotion, etc. That is why several aspects need to be considered like the pressure, work depth, versatility, and size requirements. In this regard, bio-inspiration is a good option in robot design because marine animals can serve as benchmarks with respect to different characteristics like swimming speed, efficiency, maneuverability, and stealth [18].

2.1. Speed

Bio-inspiration in locomotion or morphology seeks to achieve the speed of marine animals because they are, aside from some exceptions, faster than traditional AUVs both in terms of absolute velocity and relative velocity (the speed normalized with respect to their body length (BL)) because of their swimming system and the drag reduction of their bodies, developed by years of underwater evolution [18,19].

2.2. Efficiency

Efficiency pertains to power usage and determines the distance that can be covered and the operational duration for a specific amount of fuel or energy [18]. It can be measured with the cost of transport (COT), which quantifies the energy expenditure required to swim at a given speed and is inversely proportional to efficiency [20,21]. Equation (1) shows the mathematical expression of this parameter [22]:

$$COT \triangleq \frac{E}{mgd} = \frac{P}{mgv} \quad (1)$$

where E and P are the energy and power of the system, d and v are the distance traveled and the velocity of the vehicle, m is the mass of the system, and g is the acceleration due to gravity, for the units of measurement of the mentioned variables, the International System of Units is used.

2.3. Maneuverability and Agility

Maneuverability is the capability to change speed, direction, and location while maintaining stability and can be described as the capability to turn in a confined space; it involves fast and stable navigation even at low speeds. Maneuvering can be focused on lateral turning; that is why maximal maneuverability is usually associated with the minimum turn radius; with this definition it can be measured as the length-specific radius r_{ls} of the turn trajectory [23,24].

The agility is the rate of turn while changing directions and is measured as the change in angular velocity [25]. The concept of agility also includes the concept of maneuverability, but in this case speed agility is the ability of the vehicle to accelerate or decelerate [23].

2.4. Bio-Inspired Rajiform Underwater Robot

When talking about rajiform bio-inspiration, the most common approach is to reproduce their locomotion by trying to replicate the pectoral fin system using multiples actuators; there are some examples of this approach, like [15], where the robot has fourteen degrees of freedom, using three servomotors on each side of the fin design and with three ribs attached to the axis. In [26], the robot has pectoral fins that consist of three complex mechanisms with the goal of resembling the skeleton of the real fins. In [27], the design consists of five motors on each fin and two propellers located in the body of the robot.

The downside of these designs is the fact that the used fins are not as flexible as those of fish, resulting in lower degrees of freedom and loss of maneuverability [4,28] and the fact that multiple actuators positioned within the fins in this kind of robot may present restrictions in the design and sizing of the system, in addition to greater energy consumption.

Another approach [15] consists of modeling the oscillatory movement of the fin through the combination of a synchronized flapping movement and a pitching rotation of

the fin. In [15,29,30], the strategy used to model rajiform locomotion is the use of flexible materials to build the fin and a single actuator to move each one of them; this translates to a degree of freedom in each one of the fins; the undulation then is obtained passively. The disadvantages of these robots is that the maneuverability is decreased.

As can be seen in the prototypes mentioned above, the efforts to imitate the form of locomotion of rajiforms made them use a large number of actuators, which make the systems very complex, and therefore, important characteristics such as speediness or maneuverability are sacrificed. For this reason, the inspiration for this work was mainly based on the hydrodynamic advantages of the shape of bat rays.

According to the previously mentioned literature, bat rays exhibit lower drag and high stability, characteristics that are highly desirable for an underwater vehicle. One way to reproduce the contour of the fin is to approximate it with a series of aerodynamic profiles with gradient changes from a large profile in the center of the body to a small profile at the tip of the fin [31]. The thickness of the body should follow the dimensions of the body and the body should be flattened [32].

In the proposed design, a series of scaled NACA0012 profiles were used and a joint was added to redirect the flow through the fins, as shown in Figure 2. In this part of the design, the Fusion 360 v2.0 software was used, along with two guide profiles. The smallest chord line, located at the end of the fin, measures 10 mm, while the longest is 216 mm.

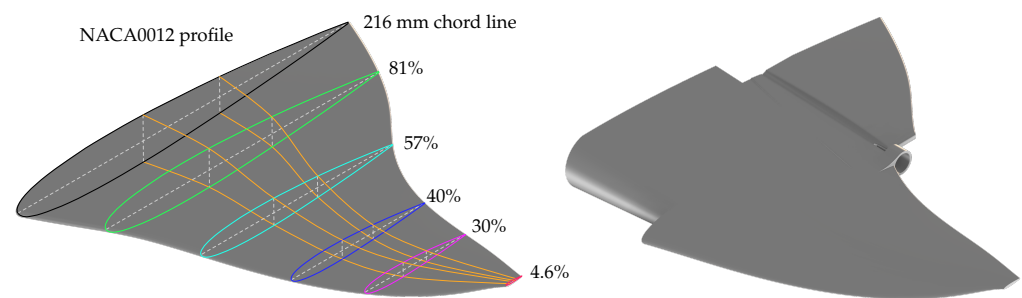


Figure 2. Design of the robot fins based on the NACA0012 profile.

The NACA0012 profile allows us to simplify the vehicle model as it is a symmetrical profile. In Figure 3, two simulations can be observed, carried out in Comsol Multiphysics, that show the behavior of the profile when a water flow at 1 m/s passes around its geometry. Since it is a symmetrical profile, the speed of the fluid passing above it is the same as that passing below it, this is also the case for pressure. It is worth mentioning that this simulation was carried out for an angle of attack of 0° , generating a cancellation in the lift forces.

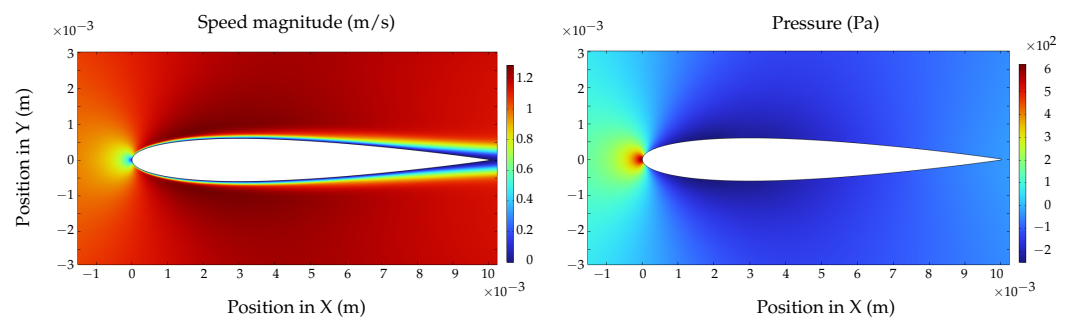


Figure 3. Simulation in Comsol Multiphysics 6.2 to observe the behavior of surrounding fluid around profile NACA0012.

The locomotion of our prototype is based on two thrusters and two control surfaces (fin tips) manipulated by a servomotor in each one. Because the propeller is located in front of the fin, it is possible to modify the direction of the fluid through the control surfaces.

Figure 4 shows three general cases of how the flow is redirected to modify the motion of the vehicle. These simulations were carried out using the Flow Simulation plugin of the SolidWorks 2023 software. This mechanism allows different forces and torques to be generated, as shown in the vehicle model section.

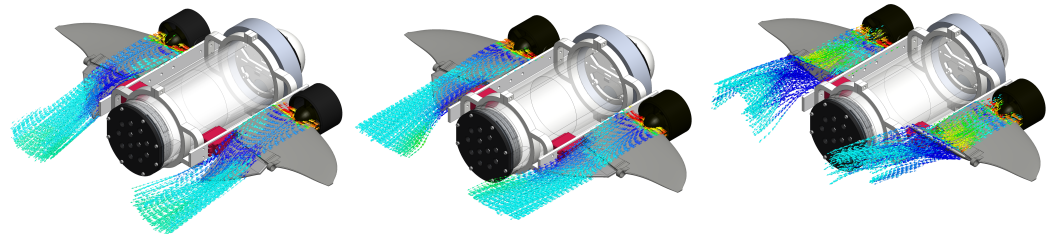


Figure 4. Simulation of the modification of fluid flow direction around the fin through the action of control surfaces.

3. Modeling, Simulation, and Control

The platform proposed in the previous section is characterized by having two thrusters and two fins that are placed symmetrically, which we refer to with the index $i \in \{1, 2\}$, where 1, 2 represent the left and the right sides, respectively. Figure 5 shows the structure of the platform and the coordinate systems used.

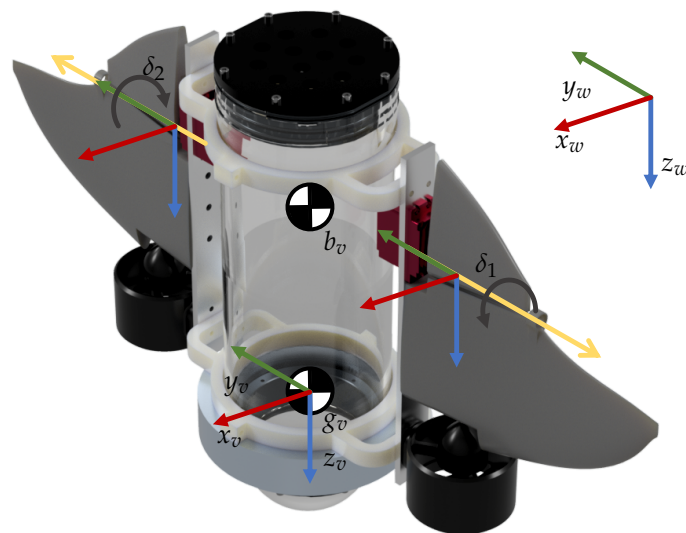


Figure 5. Locations of the coordinate systems for the dynamic analysis.

In Figure 5, the unitary vectors $x_w, y_w,$ and z_w form the coordinate system of the world O_w , similarly $x_v, y_v,$ and z_v form the coordinate system of the vehicle O_v , the center of gravity (CoG) of the vehicle is denoted as g_v and it is located at the origin of O_v , the center of buoyancy (CoB) of the vehicle is denoted as b_v , and the angle of the fins is represented by δ_i .

To define the mathematical model of the system, a simplified notation is defined for position r , linear velocity v , angular velocity ω , linear acceleration a , and angular acceleration α ; this notation uses only one subscript, i.e., r_i denotes the position of origin O_i relative to the world frame O_w expressed in local frame O_i . An explicit notation is defined for the general case, this notation uses two subscripts j/i , which indicate the related frames, and one superscript k , showing the frame used to express the quantity, i.e., $r_{j/i}^k$ denotes the relative position of origin O_j relative to frame O_i expressed in frame O_k .

The notation for rotations is defined as $R_{j/i}$, which denotes the rotation matrix of origin O_j relative to O_i , then it can be used to transform vectors in O_i to O_j .

3.1. Mathematical Model

The dynamic model of the UAV can be obtained by applying the Newton–Euler methodology through an analysis of the forces and torques acting on the vehicle. In this work, the entire structure has been considered as a particle because the weight of the fin tips, compared to the mass of the vehicle, is very small.

The relation between the total force F_v and moment N_v applied to the vehicle’s CoG and the movement generated can be expressed in frame O_v , as defined in Equation (2):

$$F_v = m_v a_v \tag{2a}$$

$$N_v = I_v \alpha_v + \omega_v \times (I_v \omega_v) \tag{2b}$$

where m_v and I_v represent the mass and inertia matrix of the vehicle, measured at the CoG of the vehicle [33].

The total force F_v and moment N_v are calculated in terms of the external forces of the environment and actuation forces of the vehicle, as defined in Equation (3):

$$F_v = f_g + f_b + f_a + f_d + f_p \tag{3a}$$

$$N_v = n_g + n_b + n_a + n_d + n_p \tag{3b}$$

where f_g and n_g represent the force and moment produced by gravity on the vehicle; f_b and n_b represent the force and moment produced by the buoyancy of the vehicle; f_a and n_a represent the force and moment produced by the added mass of the vehicle; f_d and n_d represent the force and moment produced by the drag of the vehicle; and f_p and n_p represent the force and moment produced by the propeller thrusts of the vehicle. All forces and moments are defined relative to frame O_v .

Each one of the elements in Equation (3) is defined in the next subsections.

3.1.1. Gravitational Forces

The gravitational force of the vehicle f_g , expressed in O_v , is defined in Equation (4); f_g does not produce a moment because it is calculated at the vehicle’s CoG:

$$f_g = m_v g R_{v/w} z_w \tag{4a}$$

$$n_g = 0 \tag{4b}$$

where g is the acceleration due to gravity.

3.1.2. Buoyancy Forces

The buoyancy force f_b is proportional to the mass of the fluid displaced by a moving body, in the opposite direction to the gravitational force [34]; by Archimedes’ principle it is defined as follows in Equation (5):

$$f_b = -m_{f_v} g R_{v/w} z_w \tag{5a}$$

$$n_b = r_{b_v/v}^v \times f_b \tag{5b}$$

where m_{f_v} is the mass of the fluid displaced by the vehicle, calculated as $m_{f_v} = \rho_{f_l} \nabla_v$, where ρ_{f_l} is the density of the fluid and ∇_v the volume of the fluid displaced by the vehicle. The position of the center of buoyancy relative to O_v is denoted as $r_{b_v/v}^v$.

3.1.3. Added Mass Forces

When a submerged body moves, it must displace a volume of the fluid that surrounds it. In the hydrodynamics field, this phenomenon can be modeled as a virtual mass added to the system [35].

The mathematical expression of added mass forces highly depends on the geometry, velocity of the vehicle, frequency of the fluid, etc.; when considering a symmetric body and irrotational ocean currents, it can be approximated as shown in Equation (6):

$$f_a = -m_{f_v} a_{vr} \tag{6a}$$

$$n_a = -I_{a_v} \alpha_v - \omega_v \times (I_{a_v} \omega_v) \tag{6b}$$

where I_{a_v} is an inertia matrix due to the added vehicle mass and a_{vr} is the acceleration of the vehicle relative to the surrounding fluid, defined as $a_{vr} = a_v - R_{v/w} a_{fl}$, where a_{fl} is the acceleration of the fluid expressed in O_w . Considering an irrotational fluid implies $\omega_{fl} = 0$.

3.1.4. Damping Forces

Another hydrodynamic effect is the damping caused by the fluid’s viscosity that causes dissipative forces of drag (profile and superficial friction) and lifts that act on the body’s center [36]. The lift forces are orthogonal to the velocity of the fluid, and the drag forces are parallel to the velocity of the fluid and act on the CoM of the body [37].

Damping forces and moments are nonlinear and coupled; the following Equation (7) represents only the linear decoupled part of these phenomena:

$$f_d = -d_v v_{vr} \tag{7a}$$

$$n_d = -D_v \omega_v \tag{7b}$$

where D_v and d_v represent the linear coefficients of the damping forces.

3.1.5. Propeller Forces

The propeller force f_{p_i} is defined as shown in Equation (8):

$$f_{p_i} = f_{t_i} R_{y,\delta_i} z_v \tag{8a}$$

$$n_{p_i} = r_{p_i/v}^v \times f_{p_i} \tag{8b}$$

where f_{t_i} is the force generated by thruster t_i and R_{y,δ_i} is the rotation matrix around the y -axis that defines the orientation of fin i , with a rotation δ_i (rad). The position where f_{p_i} is applied to the vehicle, relative to O_v , is denoted as $r_{p_i/v}^v$.

3.2. Simulation

Using Equations (2)–(8), the dynamic model can be solved to obtain the acceleration vector relative to O_v , denoted by $\dot{v} = [a_v \ \alpha_v]^T$; the numerical integration of \dot{v} is used to calculate the velocity vector $v = [v_v \ \omega_v]^T$; however, the integration of v has no physical sense [35].

The pose of the vehicle relative to O_w is denoted by $\eta = [\eta_1 \ \eta_2]^T$, where $\eta_1 = [x_v \ y_v \ z_v]^T$ is the position and $\eta_2 = [\phi_v \ \theta_v \ \psi_v]^T$ is the attitude.

The relation between $\dot{\eta}$ and v is expressed as shown in Equation (9) [35]:

$$\begin{bmatrix} \dot{\eta}_1 \\ \dot{\eta}_2 \end{bmatrix} = J(\eta_2) \begin{bmatrix} v_v \\ \omega_v \end{bmatrix} = \begin{bmatrix} J_1(\eta_2) & 0_{3 \times 3} \\ 0_{4 \times 3} & J_2(\eta_2) \end{bmatrix} \begin{bmatrix} v_v \\ \omega_v \end{bmatrix} \tag{9}$$

where $J_1(v_2) = R_{w/v}$ and $J_2(v_2)$ is defined depending on the rotation sequence used to define the attitude.

Transformation matrix $J(v_2)$ has singularities, which depends on the chosen rotation sequence [38]; this inconvenience can be avoided by keeping the vehicle around a safe configuration; however, in this project this is not an option because it is desired that the vehicle can submerge and emerge vertically, and then, navigate horizontally to take advantage of the bio-inspired morphology.

An alternative relation to the one presented in Equation (9) is found by expressing the attitude using quaternions, which is shown in Equation (10):

$$\begin{bmatrix} \dot{\eta}_1 \\ \dot{\eta}_{2,q} \end{bmatrix} = E(\eta_{2,q}) \begin{bmatrix} v_v \\ \omega_v \end{bmatrix} = \begin{bmatrix} E_1(\eta_{2,q}) & 0_{3 \times 3} \\ 0_{3 \times 3} & E_2(\eta_{2,q}) \end{bmatrix} \begin{bmatrix} v_v \\ \omega_v \end{bmatrix} \tag{10}$$

where $\eta_{2,q} = [\epsilon_1 \ \epsilon_2 \ \epsilon_3 \ \eta_q]^T$ denotes the attitude expressed in the quaternion representation, which is obtained using the rotation sequence ‘‘XYZ’’.

The transformation matrices $E_1(\eta_{2,q})$ and $E_2(\eta_{2,q})$ are defined as shown in Equation (11):

$$E_1(\eta_{2,q}) = \begin{bmatrix} 1 - 2(\epsilon_2^2 + \epsilon_3^2) & 2(\epsilon_1\epsilon_2 - \epsilon_3\eta_q) & 2(\epsilon_1\epsilon_3 + \epsilon_2\eta_q) \\ 2(\epsilon_1\epsilon_2 + \epsilon_3\eta_q) & 1 - 2(\epsilon_1^2 + \epsilon_3^2) & 2(\epsilon_2\epsilon_3 - \epsilon_1\eta_q) \\ 2(\epsilon_1\epsilon_3 - \epsilon_2\eta_q) & 2(\epsilon_2\epsilon_3 + \epsilon_1\eta_q) & 1 - 2(\epsilon_1^2 + \epsilon_2^2) \end{bmatrix} \tag{11a}$$

$$E_2(\eta_{2,q}) = \frac{1}{2} \begin{bmatrix} \eta_q & -\epsilon_3 & \epsilon_2 \\ \epsilon_3 & \eta_q & -\epsilon_1 \\ -\epsilon_2 & \epsilon_1 & \eta_q \\ -\epsilon_1 & -\epsilon_2 & -\epsilon_3 \end{bmatrix} \tag{11b}$$

The attitude $\eta_{2,q}$ can be obtained by numerical integration, and then, converted to Euler angles to obtain η_2 ; this approach is helpful because $E_1(\eta_{2,q}^{-1})$ is used instead of $R_{v/w}$ in the equations of motion, but η_2 is needed to define the tracking error.

The procedure described in this subsection is summarized in the block diagram shown in Figure 6.

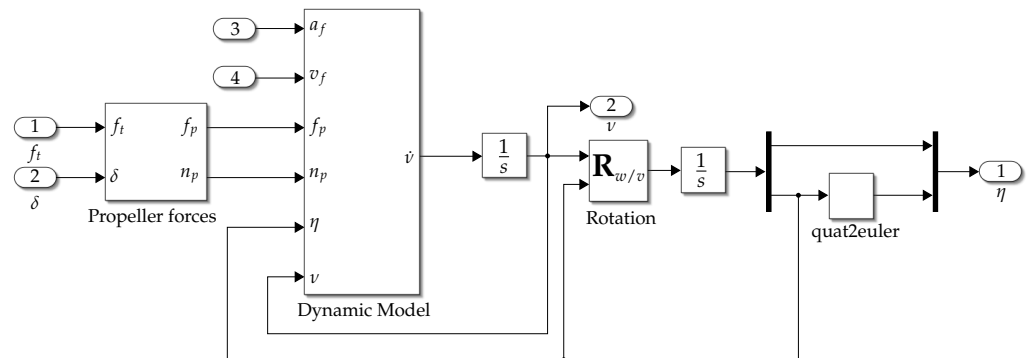


Figure 6. Numerical integration of the proposed mathematical model.

3.3. Control

The control problem is defined as a simultaneous forward velocity- and attitude-tracking problem. The proposed control law is a classical proportional–integral (PI) scheme, as shown in Equation (12):

$$C = \begin{bmatrix} \mathbf{f}_{p,z} \\ \mathbf{n}_{p,x} \\ \mathbf{n}_{p,y} \\ \mathbf{n}_{p,z} \end{bmatrix} = k_p \begin{bmatrix} v_{d,z} - v_{v,z} \\ \phi_d - \phi_v \\ \theta_d - \theta_v \\ \psi_d - \psi_v \end{bmatrix} + k_i \int \begin{bmatrix} v_{d,z} - v_{v,z} \\ \phi_d - \phi_v \\ \theta_d - \theta_v \\ \psi_d - \psi_v \end{bmatrix} dt \tag{12}$$

note that $\mathbf{f}_{p,x}$ and $\mathbf{f}_{p,y}$ are not part of control vector C .

If Equation (8) calculates f_p and n_p as a function of f_{t_i} and δ_i , then it is called a direct actuation model (DAM). When implementing control signals C as shown in Equation (12), an inverse actuation model (IAM) is needed to define actuation references given desired forces and moments.

The calculation of IAM is not straightforward because Equation (8) is nonlinear; the explicit equations for the proposed platform can be obtained by considering $r_{p_i/g_v}^v = [0, \mp r_{p,y}, -r_{p,z}]^T$ for $i = 1, 2$, as shown in Equation (13):

$$f_p = f_{p1} + f_{p2} = \begin{bmatrix} f_{p,x} \\ f_{p,y} \\ f_{p,z} \end{bmatrix} = \begin{bmatrix} f_{t1} \sin \delta_1 + f_{t2} \sin \delta_2 \\ 0 \\ f_{t1} \cos \delta_1 + f_{t2} \cos \delta_2 \end{bmatrix} \tag{13a}$$

$$n_p = n_{p1} + n_{p2} = \begin{bmatrix} n_{p,x} \\ n_{p,y} \\ n_{p,z} \end{bmatrix} = \begin{bmatrix} -r_{p,y}(f_{t1} \cos \delta_1 - f_{t2} \cos \delta_2) \\ -r_{p,z}(f_{t1} \sin \delta_1 + f_{t2} \sin \delta_2) \\ r_{p,y}(f_{t1} \sin \delta_1 - f_{t2} \sin \delta_2) \end{bmatrix} \tag{13b}$$

An approximated result can be obtained by considering that the fins have a small range of movement $\delta_i \in (-20^\circ, 20^\circ)$, then $\sin \delta_i \approx \delta_i$ y $\cos \delta_i \approx 1$, which has an approximate error of 2%. Using these considerations, the IAM is calculated as shown in Equation (14):

$$f_{t_{1,2}} = \frac{r_{p,y} f_{p,z} \mp n_{p,x}}{2r_{p,y}} \tag{14a}$$

$$\delta_{1,2} = \frac{-r_{p,y} n_{p,y} \pm r_{p,z} n_{p,z}}{2r_{p,y} r_{p,z} f_{t_{1,2}}} \tag{14b}$$

Note that $\delta_{1,2}$ is not defined when $f_{t_{1,2}} = 0$; this is evident because when there is no flow through the fin, the fin angle does not affect the actuation. When this condition is detected, the reference for $\delta_{1,2}$ is kept in its last known state using a memory block.

Figure 7 shows the implementation of the control block; note that saturation blocks are added after actuator signals according to the physical limitation of the propellers and fins.

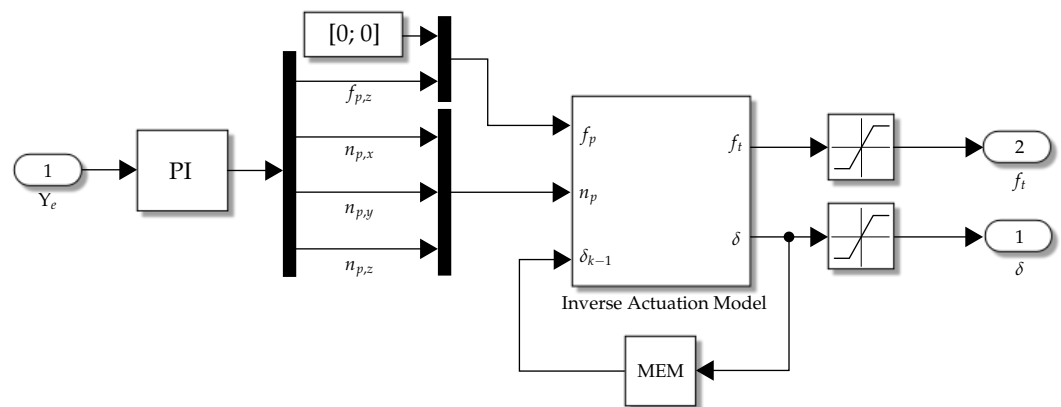


Figure 7. Numerical implementation of the control strategy.

4. Results

In this section, simulation and experimental results are presented; the complete control loop is presented in the blocks diagram shown in Figure 8, where the implementation of the vehicle block is shown in Figure 6 for the simulation and the implementation of the control block is shown in Figure 7.

4.1. Simulation Results

The simulation results were obtained using Matlab R2023b, Simulink and the VR toolbox for visualization. The selected ODE solver was the fourth-order Runge–Kutta (ODE4), with fixed time step $t_s = 0.001$ s. Simulation results are independent of the chosen step time; this was verified by running simulations using different values in the range $t_s \in (0.001, 0.1)$, where the maximum difference in position was 0.1065% and the maximum difference in orientation was 2.7184%.

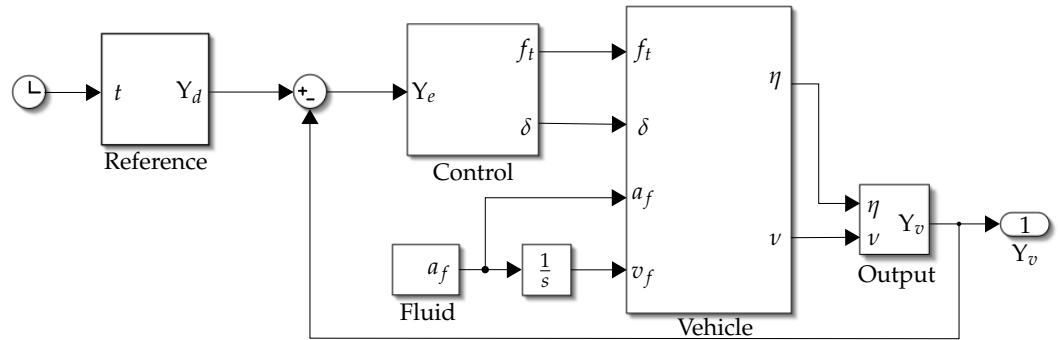


Figure 8. Blocks diagram of the simulator designed in Matlab R2023b and Simulink.

The mass and propulsion parameters of the vehicle used for simulation are shown in Table 1; the hydrodynamic parameters of the vehicle are shown in Table 2, they were obtained using Flow Simulation plugin of the SolidWorks 2023 software.

Table 1. Mass and propulsion parameters of the vehicle.

m_v (kg)	I_{g_v} (kg m ²)	$r_{p_1/v}^v$ (m)	$r_{p_2/v}^v$ (m)
3.956	$\begin{bmatrix} 0.063 & 0 & 0 \\ 0 & 0.045 & 0 \\ 0 & 0 & 0.026 \end{bmatrix}$	$\begin{bmatrix} 0 \\ -0.15 \\ -0.084 \end{bmatrix}$	$\begin{bmatrix} 0 \\ 0.15 \\ -0.084 \end{bmatrix}$

Table 2. Hydrodynamic parameters of the vehicle.

m_{f_v} (kg)	I_{f_v} (kg m ²)	$r_{b_v/v}^v$ (m)	d_v (Ns/m)	D_v (Nms/rad)
4.3	$\begin{bmatrix} 0.055 & 0 & 0 \\ 0 & 0.038 & 0 \\ 0 & 0 & 0.023 \end{bmatrix}$	$\begin{bmatrix} 0 \\ 0 \\ -0.009 \end{bmatrix}$	$\begin{bmatrix} 100 & 0 & 0 \\ 0 & 10 & 0 \\ 0 & 0 & 10 \end{bmatrix}$	$\begin{bmatrix} 1 & 0 & 0 \\ 0 & 0.9 & 0 \\ 0 & 0 & 5 \end{bmatrix}$

The saturation for the thruster’s force is 20 N and the saturation for the fin’s angle is $\pi/4$ rad. The fluid is considered at rest when $a_{fl} = 0$. The initial conditions $v(0)$ and $\eta_q(0)$ are configured in the integration blocks shown in Figure 6.

The gain matrices introduced in Equation (12) are defined as shown in Equation (15).

$$k_p = \begin{bmatrix} 100 & 0 & 0 & 0 \\ 0 & 15 & 0 & 0 \\ 0 & 0 & 10 & 0 \\ 0 & 0 & 0 & 20 \end{bmatrix} \quad k_i = \begin{bmatrix} 30 & 0 & 0 & 0 \\ 0 & 1 & 0 & 0 \\ 0 & 0 & 0.5 & 0 \\ 0 & 0 & 0 & 5 \end{bmatrix} \quad (15)$$

The capabilities of the proposed architecture are tested using four reference trajectories, which exhibit the maneuverability of the vehicle; the references are defined using time and pose keypoints, with a linear interpolator to calculate the intermediate positions.

4.1.1. Test 1: Vertical Submerging and Emerging

The trajectory defined in Table 3 is designed to demonstrate that the vehicle is able to change its navigation style from hover to gliding, in the same way as vertical take off and landing (VTOL) flying drones [39].

Table 3. Vertical submerging and emerging test reference table.

T (s)	$v_{d,z}$ (m/s)	ϕ_d (rad)	θ_d (rad)	ψ_d (rad)
0	0	0	0	0
0.5	0.5	0	0	0
2	1	0	$\pi/2$	0
3	0.5	0	$\pi/2$	0
1	0.25	0	$\pi/4$	0
2	-1	0	0	0
0.5	0	0	0	0

The initial conditions for this test are defined by setting the vehicle at rest and located at the surface of the water, vertically, i.e., $v(0) = [0 \ 0 \ 0 \ 0 \ 0 \ 0]^T$ and $\eta_q(0) = [0 \ 0 \ 0 \ 1 \ 0 \ 0]^T$.

The tracking results for the vertical submerging and emerging test are shown in Figure 9, note that $\phi_d = 0$ and $\psi_d = 0$ because in the vertical submerging and emerging test only a trajectory for θ_d is needed.

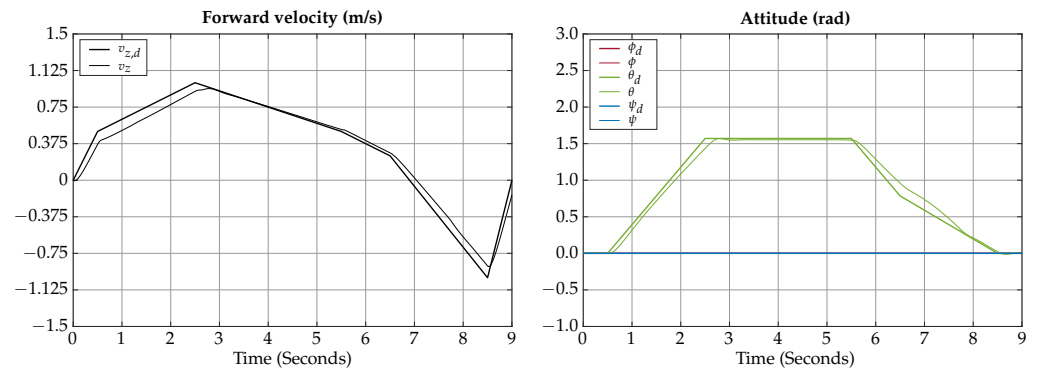


Figure 9. Vertical submerging and emerging test tracking results.

The control signals for the vertical submerging and emerging test are shown in Figure 10, note that in the vertical submerging and emerging test the control signals for the fins and thrusters are the same, for the left and right sides, in the absence of perturbations.

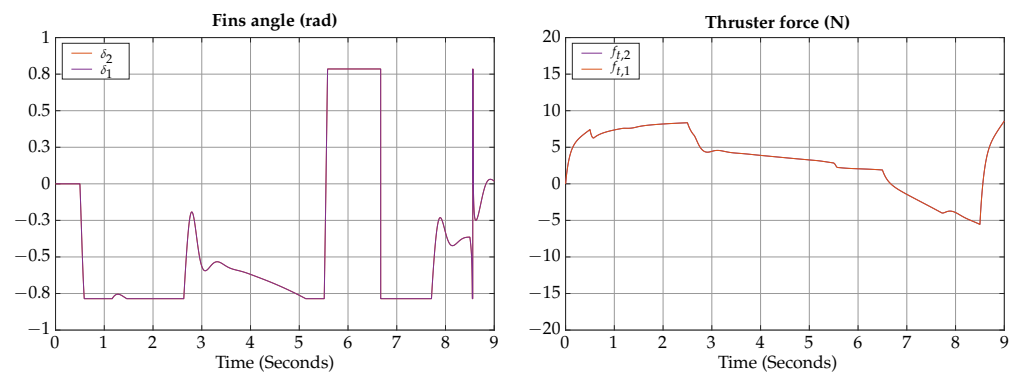


Figure 10. Vertical submerging and emerging test control signals.

The total simulation time is 9 s; the corresponding trajectory of the vertical submerging and emerging test is shown in Figure 11.

According to the simulation results of this test, the vehicle is capable of changing navigation modes within 2 s; however, the fin’s angle reaches the saturation value, indicating that the transition cannot be achieved faster.

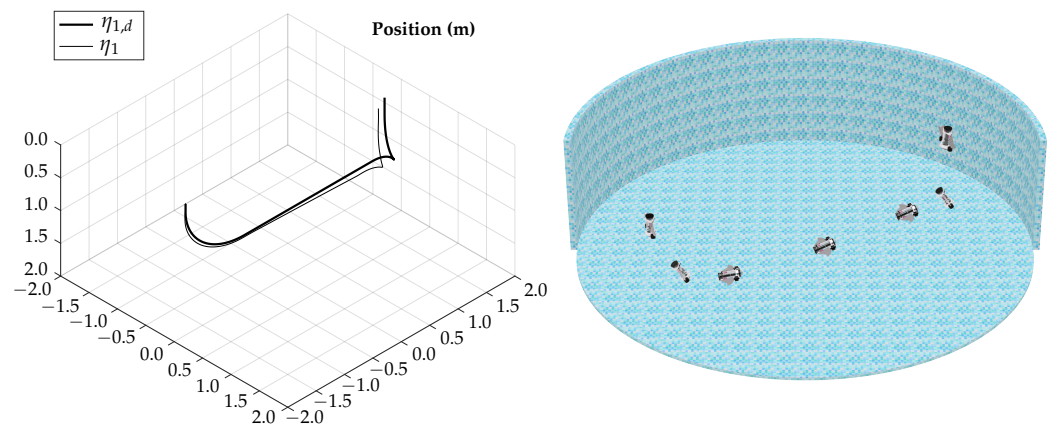


Figure 11. Vertical submerging and emerging test visualization.

4.1.2. Test 2: Horizontal Gliding

The trajectory defined in Table 4 is designed to demonstrate that the vehicle is able to control its lateral movement in gliding mode.

Table 4. Horizontal gliding test reference table.

T (s)	$v_{d,z}$ (m/s)	ϕ_d (rad)	θ_d (rad)	ψ_d (rad)
0	0	0	$\pi/2$	0
1	1	$-\pi/4$	$\pi/2$	0
1	1	$\pi/4$	$\pi/2$	0
0.75	1	$\pi/4$	$\pi/2$	0
1	1	$-\pi/4$	$\pi/2$	0
0.25	1	$-\pi/4$	$\pi/2$	0
0.25	0.5	0	$\pi/2$	0
1	0.5	0	$\pi/2$	0

The initial conditions for this test are defined by setting the vehicle at rest at 1 m below the surface of the water, horizontally, i.e., $v(0) = [0 \ 0 \ 0 \ 0 \ 0 \ 0]^T$ and $\eta_q(0) = [0 \ 0 \ 1 \ 0.7071 \ 0 \ 0.7071 \ 0]^T$.

The tracking results for the horizontal gliding test are shown in Figure 12.

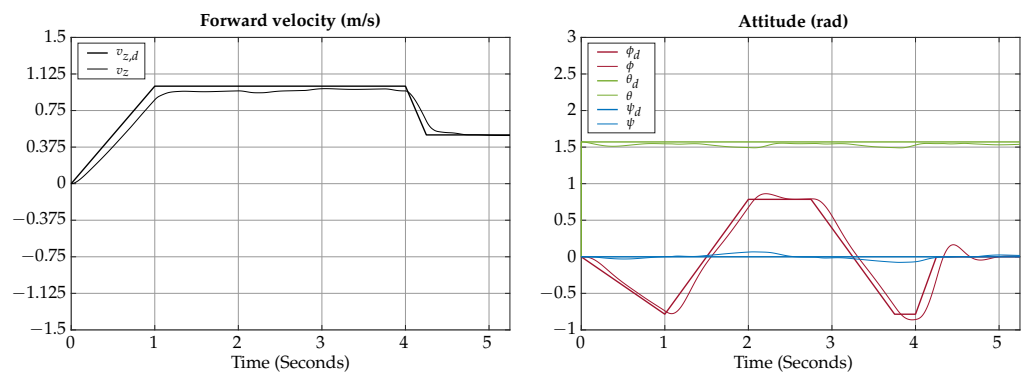


Figure 12. Horizontal gliding test tracking results.

The control signals for the horizontal gliding test are shown in Figure 13.

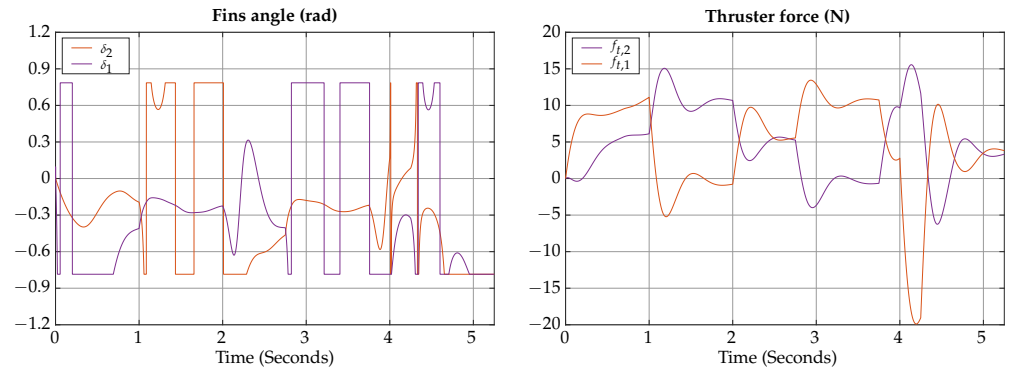


Figure 13. Horizontal gliding test control signals.

The total simulation time is 5.25 s; the corresponding trajectory of the horizontal gliding test is shown in Figure 14.

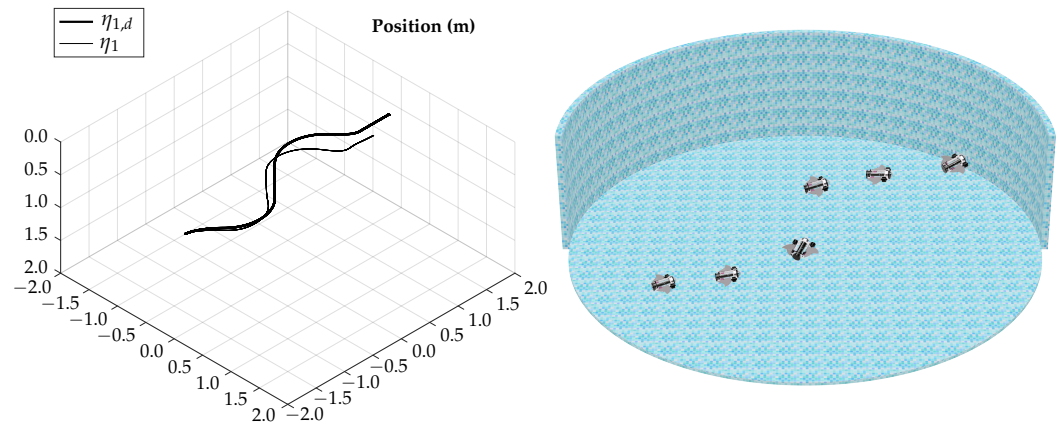


Figure 14. Horizontal gliding test visualization.

According to the simulation results of this test, the vehicle is capable of lateral movement when navigating in gliding mode; the actuation configuration allows the vehicle to control heading while maintaining the horizontal orientation.

4.1.3. Test 3: Vertical Gliding

The trajectory defined in Table 5 is designed to demonstrate that the vehicle is able to change depth in gliding mode.

Table 5. Vertical gliding test reference table.

T (s)	$v_{d,z}$ (m/s)	ϕ_d (rad)	θ_d (rad)	ψ_d (rad)
0	0	0	$\pi/2$	0
1	1	0	$5\pi/8$	0
1	1	0	$3\pi/8$	0
0.25	1	0	$3\pi/8$	0
1	1	0	$5\pi/8$	0
0.5	1	0	$5\pi/2$	0
0.5	1	0	$\pi/2$	0
0.5	1	0	$\pi/2$	0

The initial conditions for this test are defined by setting the vehicle at rest at 1 m below the surface of the water, horizontally, i.e., $v(0) = [0 \ 0 \ 0 \ 0 \ 0 \ 0]^T$ and $\eta_q(0) = [0 \ 0 \ 1 \ 0.7071 \ 0 \ 0.7071 \ 0]^T$.

The tracking results for the vertical gliding test are shown in Figure 15, note that $\phi_d = 0$ and $\psi_d = 0$ because in the vertical gliding test only a trajectory for θ_d is needed.

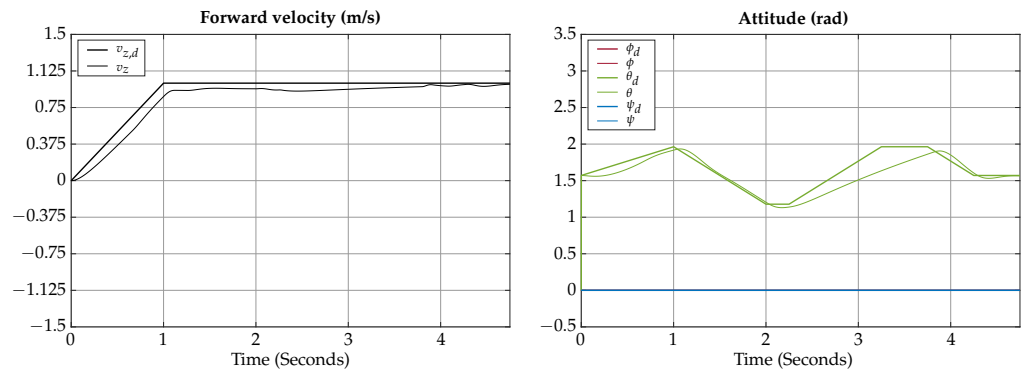


Figure 15. Vertical gliding test tracking results.

The control signals for the vertical gliding test are shown in Figure 16, note that in the vertical gliding test the control signals for the fins and thrusters are the same, for the left and right sides, in the absence of perturbations.

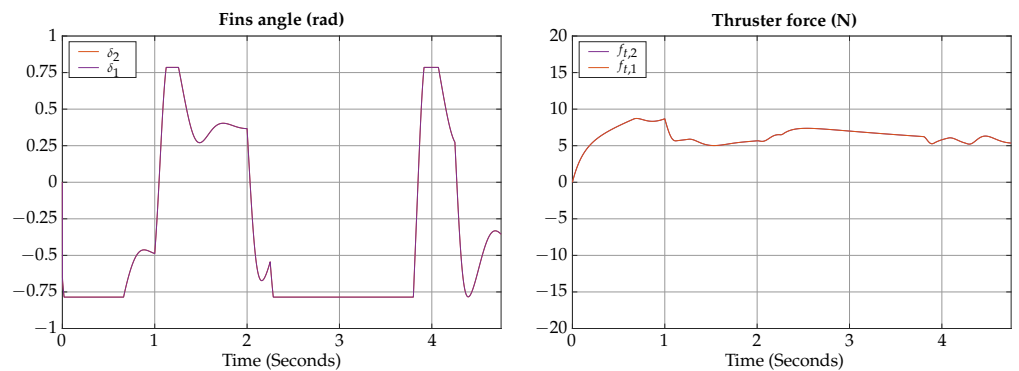


Figure 16. Vertical gliding test control signals.

The total simulation time is 4.75 s; the corresponding trajectory for the vertical gliding test is shown in Figure 17.

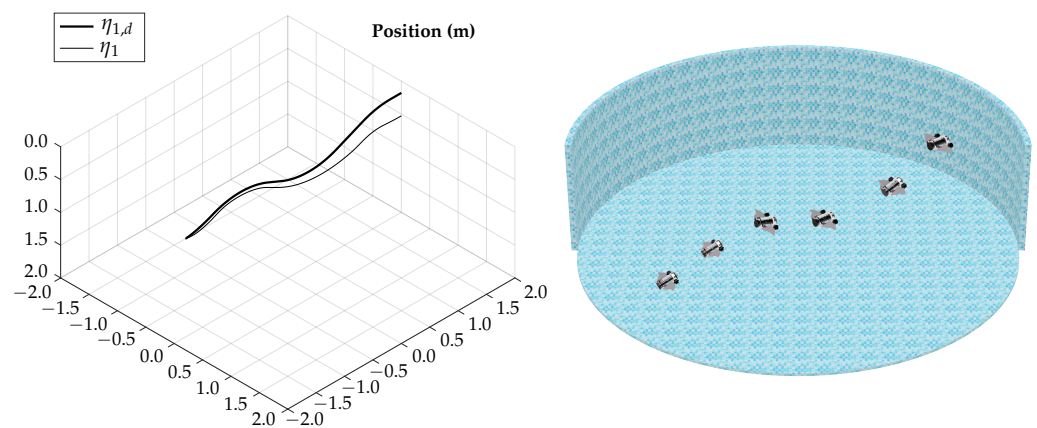


Figure 17. Vertical gliding test visualization.

According to the simulation results of this test, the vehicle is capable of controlling its depth when navigating on gliding mode; the actuation configuration allows the vehicle to change depth by following a reference in orientation.

4.1.4. Test 4: Horizontal Axial Roll

The trajectory defined in Table 6 is designed to demonstrate that the vehicle is able to control its lateral inclination in gliding mode.

Table 6. Horizontal axial roll test reference table.

T (s)	$v_{d,z}$ (m/s)	ϕ_d (rad)	θ_d (rad)	ψ_d (rad)
0	0	0	$\pi/2$	0
1	1	0	$\pi/2$	$\pi/10$
2	1	0	$\pi/2$	$-\pi/10$
1	1	0	$\pi/2$	0
0.5	1	0	$\pi/2$	0

The initial conditions for this test are defined by setting the vehicle at rest at 1 m below the surface of the water, horizontally, i.e., $v(0) = [0 \ 0 \ 0 \ 0 \ 0 \ 0]^T$ and $\eta_q(0) = [0 \ 0 \ 1 \ 0.7071 \ 0 \ 0.7071 \ 0]^T$.

The tracking results for the horizontal axial roll test are shown in Figure 18.

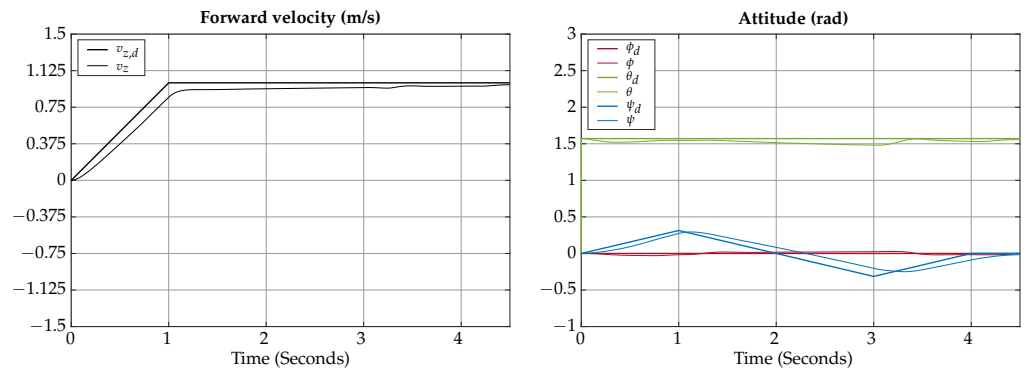


Figure 18. Horizontal axial roll test tracking results.

The control signals for the horizontal axial roll test are shown in Figure 19.

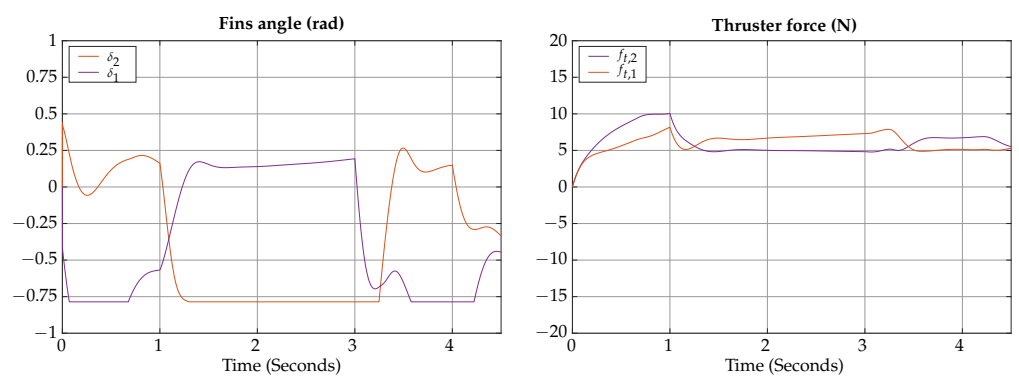


Figure 19. Horizontal axial roll test control signals.

The total simulation time is 4.5 s; the corresponding trajectory for the horizontal axial roll test is shown in Figure 20.

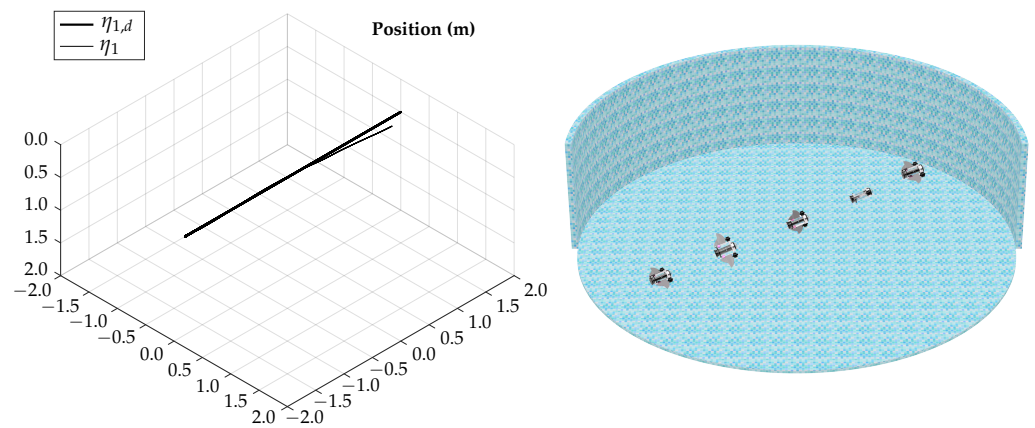


Figure 20. Horizontal axial roll test visualization.

According to the simulation results of this test, the vehicle is capable of controlling the lateral orientation when navigating on gliding mode, the actuation configuration allows the vehicle to rotate along the axis movement to compensate for possible perturbations.

4.2. Experimental Results

The experimental tests were carried out in a 4.27 m diameter pool filled with tap water; communication with the ROV was implemented through an ethernet cable and control signals were user-defined using a commercial joystick; the control and orientation signals were recorded using ROS middleware.

4.2.1. Test 1: Vertical Submerging and Emerging

This test is designed to demonstrate, using experimental results, that the proposed platform is able to change its navigation style from hover to gliding via teleoperation commands defined by a user.

The control signals for the vertical submerging and emerging experimental test are presented in Figure 21.

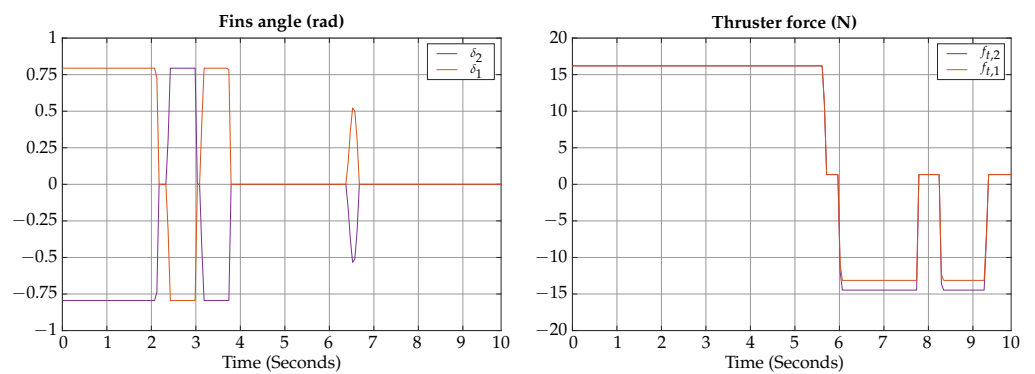


Figure 21. Vertical submerging and emerging experimental test control signals.

The measured angles for the attitude of the robot during the vertical submerging and emerging experimental test are shown in Figure 22; also, a photographic sequence is shown where the experimental trajectory of the robot can be observed.

According to the experimental results of this test, the vehicle can be teleoperated for changing navigation modes; the results are similar to the ones obtained by simulation, confirming that the vehicle can change from hover to gliding mode in about 2 s.

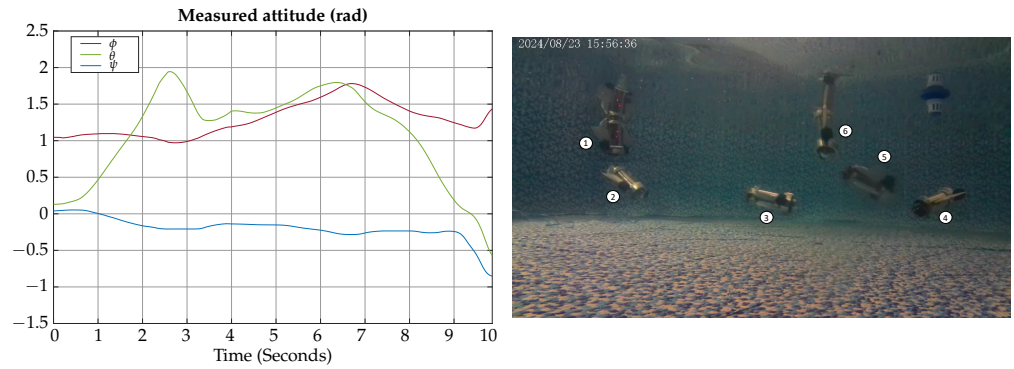


Figure 22. Vertical submerging and emerging experimental test attitude signals. The circled numbers represent the sequence of the movement.

4.2.2. Test 2: Horizontal Gliding

This test is designed to demonstrate, using experimental results, that the proposed platform is able to control its lateral movement in gliding mode via teleoperation commands defined by a user.

The control signals for the vertical gliding experimental test are presented in Figure 23.

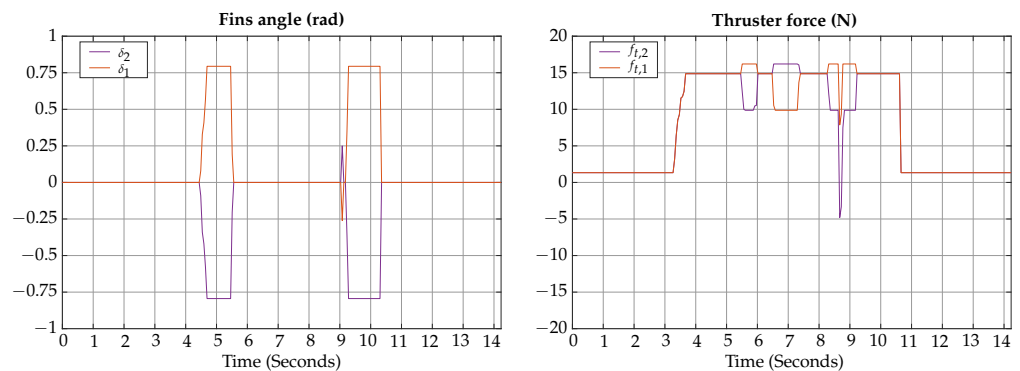


Figure 23. Horizontal gliding experimental test control signals.

The measured angles for the attitude of the robot during the horizontal gliding experimental test are shown in Figure 24; also, a photographic sequence is shown where the experimental trajectory of the robot can be observed.

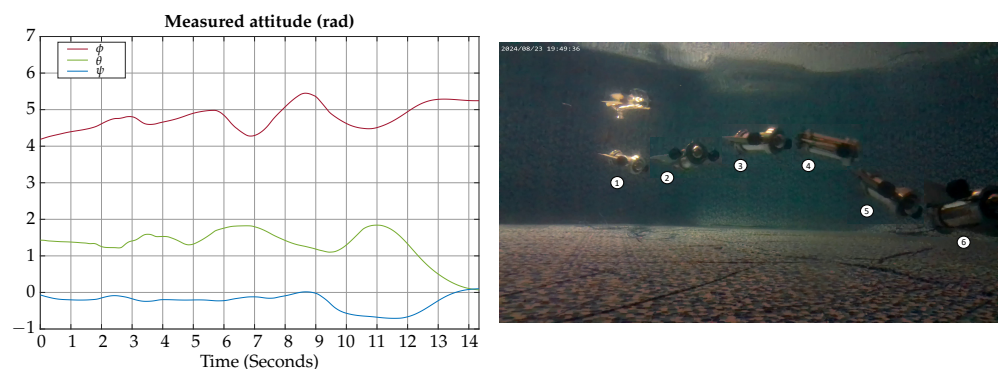


Figure 24. Horizontal gliding experimental test attitude signals. The circled numbers represent the sequence of the movement.

According to the experimental results of this test, the vehicle can be teleoperated to change lateral heading when moving in gliding mode; however, it requires practice to correctly teleoperate the horizontal and vertical motion simultaneously.

4.2.3. Test 3: Vertical Gliding

This test is designed to demonstrate, using experimental results, that the proposed platform is able to change depth in gliding mode via teleoperation commands defined by a user.

The control signals for the vertical gliding experimental test are presented in Figure 25.

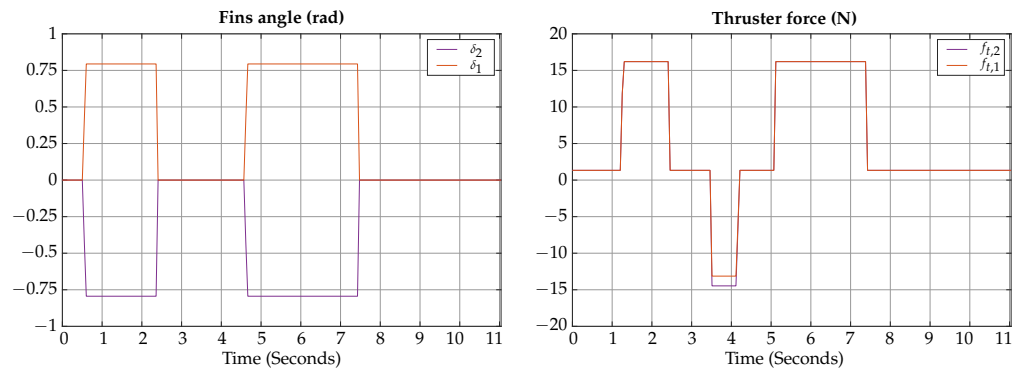


Figure 25. Vertical gliding experimental test control signals.

The measured angles for the attitude of the robot during the vertical gliding experimental test are shown in Figure 26; also, a photographic sequence is shown where the experimental trajectory of the robot can be observed.

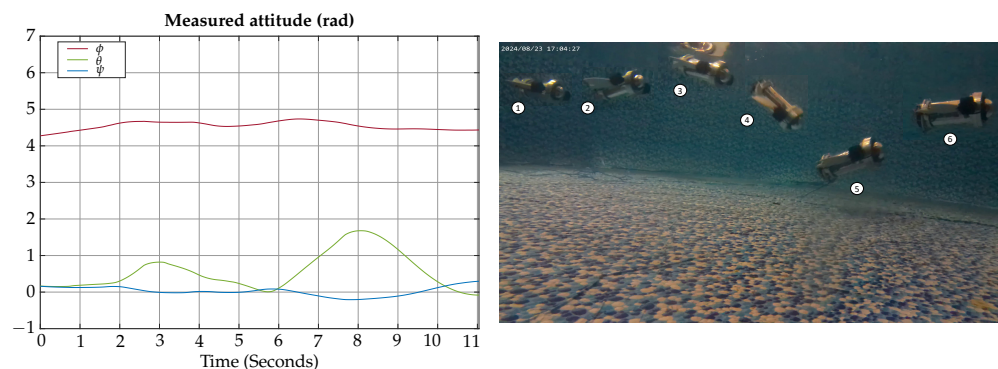


Figure 26. Vertical gliding experimental test attitude signals. The circled numbers represent the sequence of the movement.

According to the experimental results of this test, the vehicle can be teleoperated to change depth when moving in glide mode; however, due to the location of the center of buoyancy relative to the center of gravity, it requires less torque to move downwards than upwards, so the movement is not symmetrical.

5. Discussion

The simulation results show that the proposed vehicle can be teleoperated in gliding mode to follow reference orientations, as presented in Figures 9, 12, 15, and 18; however, the position of the vehicle may differ from the expected trajectory if the delay time of the transient respond is not short enough or if the actuators reach saturation values, as shown in Figures 11, 14, 17, and 20.

The experimental results, presented in Figures 22, 24, and 26, show that the platform can be challenging to teleoperate in a reduced space; one reason is that the degrees of freedom of the vehicle are highly coupled, as can be seen in Equations (13) and (14), so it is necessary to implement full pose control so the teleoperation process becomes more suitable for real-world scenarios.

Based on the simulation and experimental results, it is concluded that the proposed bio-inspired design is highly efficient and maneuverable, suitable for inspection and mapping applications. Figure 27 shows a comparison of different bio-inspired vehicles considering cost of transportation and steering speed against cruising speed. According to this comparison, the proposed prototype has a competitive cost of transportation when compared to vehicles inspired by different marine creatures, with an outstanding maneuverability, as seen in the comparison of steering speed.

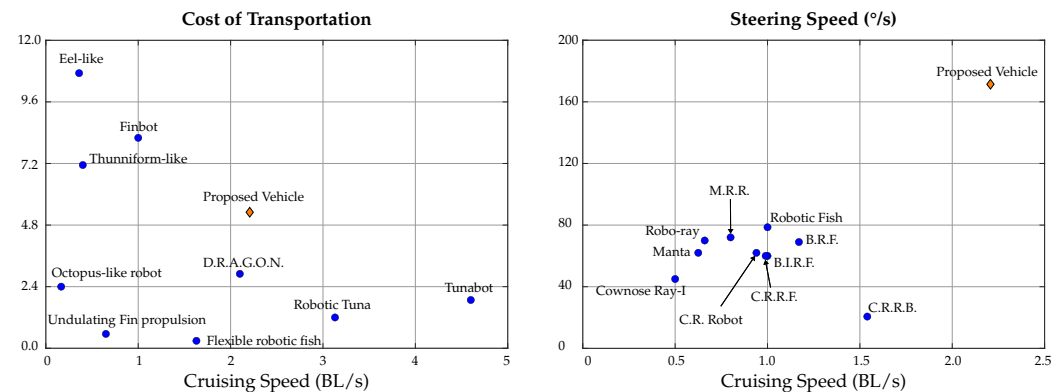


Figure 27. Comparison of cost of transportation and steering speed of different bio-inspired underwater vehicles: C.R.R.B. [15], Manta [16], Thunniform-like [22], M.R.R. [26], Octopus-like robot [40], Eel-like [41], Undulating Fin propulsion [42], Finbot [43], Flexible robotic fish [44], D.R.A.G.O.N. [45], Robotic Tuna [46], Tunabot [47], Cownose Ray-I [48], Robo-ray [49], C.R. Robot [50], Robotic Fish [51], C.R.R.F. [52], B.I.R.F. [53] and B.R.F. [54].

Although flapping is a highly efficient form of propulsion, it provides poor maneuverability compared with the proposed hybrid design that combines thrusters and fins.

The vehicle performance can be improved by reducing drag during glide mode; this can be achieved by modifying the design of the electronic capsule; a reduction in drag will increase the cruising speed, which in turn reduces the transport cost. The steering speed can also be improved by increasing the area of the mobile section of the fins and/or adding another joint for better fluid redirection.

In addition to the mechanical improvements that can be implemented on the platform, there is plenty of work that can be performed regarding the automatic control and localization strategies that can be designed using the proposed mathematical model.

In conclusion, the proposed underwater ROV design, based on traditional thrusters and bio-inspired articulated fins, is an efficient platform capable of vertical submerging and emerging, is an energy efficient vehicle compared with similar projects, and exhibits outstanding maneuverability. The proposed architecture, considered as an experimental control platform, is a challenging system for the design of automatic controllers but also attractive for real-world applications such as exploration and mapping.

Author Contributions: Conceptualization, E.M.-C., S.A.M.-R. and R.S.N.-C.; methodology, E.D.A.-Y. and L.M.A.-L.; software, E.M.-C. and S.A.M.-R.; validation, E.M.-C., S.A.M.-R. and R.S.N.-C.; formal analysis, E.M.-C., S.A.M.-R. and R.S.N.-C.; investigation, E.M.-C., S.A.M.-R., R.S.N.-C., E.D.A.-Y., L.M.A.-L. and J.H.-V.; resources, E.M.-C.; data curation, E.M.-C., S.A.M.-R., R.S.N.-C., and E.D.A.-Y.; writing—original draft preparation, E.M.-C. and R.S.N.-C.; writing—review and editing, S.A.M.-R., E.D.A.-Y., L.M.A.-L. and J.H.-V.; visualization, E.M.-C. and J.H.-V.; supervision, R.S.N.-C. and E.D.A.-Y.; project administration, R.S.N.-C. All authors have read and agreed to the published version of the manuscript.

Funding: This research received no external funding.

Data Availability Statement: Data are contained within the article.

Conflicts of Interest: The authors declare no conflict of interest.

References

1. Yu, X.; Tao, J.; Berilla, J. A bio-inspired flow sensor. In *Nanosensors, Biosensors, and Info-Tech Sensors and Systems 2010*; Varadan, V.K., Ed.; SPIE: St Bellingham, WA, USA, 2010.
2. Valdivia y Alvarado, P.; Subramaniam, V.; Triantafyllou, M. Design of a bio-inspired whisker sensor for underwater applications. In Proceedings of the SENSORS, 2012 IEEE, Taipei, Taiwan, 28–31 October 2012; pp. 1–4. [\[CrossRef\]](#)
3. Xu, P.; Liu, J.; Liu, X.; Wang, X.; Zheng, J.; Wang, S.; Chen, T.; Wang, H.; Wang, C.; Fu, X.; et al. A bio-inspired and self-powered triboelectric tactile sensor for underwater vehicle perception. *Npj Flex. Electron.* **2022**, *6*, 25. [\[CrossRef\]](#)
4. Sun, B.; Li, W.; Wang, Z.; Zhu, Y.; He, Q.; Guan, X.; Dai, G.; Yuan, D.; Li, A.; Cui, W.; et al. Recent Progress in Modeling and Control of Bio-Inspired Fish Robots. *J. Mar. Sci. Eng.* **2022**, *10*, 773. [\[CrossRef\]](#)
5. Manduca, G.; Santaera, G.; Miraglia, M.; Jansen Van Vuuren, G.; Dario, P.; Stefanini, C.; Romano, D. A bioinspired control strategy ensures maneuverability and adaptability for dynamic environments in an underactuated robotic fish. *J. Intell. Robot. Syst.* **2024**, *110*, 69. [\[CrossRef\]](#)
6. Heinen, Y.; Tanev, I.; Kimura, T. The Effect of a Limited Underactuated Posterior Joint on the Speed and Energy Efficiency of a Fish Robot. *Appl. Sci.* **2024**, *14*, 5010. [\[CrossRef\]](#)
7. Luo, Y.; Xiao, Q.; Zhu, Q.; Pan, G. Pulsed-jet propulsion of a squid-inspired swimmer at high Reynolds number. *Phys. Fluids* **2020**, *32*, 111901. [\[CrossRef\]](#)
8. Bianchi, G.; Lanzetti, L.; Mariana, D.; Cinquemani, S. Bioinspired design and experimental validation of an aquatic snake robot. *Biomimetics* **2024**, *9*, 87. [\[CrossRef\]](#)
9. Zhang, J.; Chen, Y.; Liu, Y.; Gong, Y. Dynamic modeling of underwater snake robot by hybrid rigid-soft actuation. *J. Mar. Sci. Eng.* **2022**, *10*, 1914. [\[CrossRef\]](#)
10. Yang, Y.; Chu, C.; Jin, H.; Hu, Q.; Xu, M.; Dong, E. Design, modeling, and control of an Aurelia-inspired robot based on SMA artificial muscles. *Biomimetics* **2023**, *8*, 261. [\[CrossRef\]](#)
11. Muralidharan, M.; Saini, P.; Ameta, P.; Palani, I.A. Bio-inspired soft jellyfish robot: A novel polyimide-based structure actuated by shape memory alloy. *Int. J. Intell. Robot. Appl.* **2023**, *7*, 671–682. [\[CrossRef\]](#)
12. Soliman, M.; Mousa, M.A.; Saleh, M.A.; Elsamanty, M.; Radwan, A.G. Modelling and implementation of soft bio-mimetic turtle using echo state network and soft pneumatic actuators. *Sci. Rep.* **2021**, *11*, 12076. [\[CrossRef\]](#)
13. van der Geest, N.; Garcia, L.; Borret, F.; Nates, R.; Gonzalez, A. Soft-robotic green sea turtle (*Chelonia mydas*) developed to replace animal experimentation provides new insight into their propulsive strategies. *Sci. Rep.* **2023**, *13*, 11983. [\[CrossRef\]](#) [\[PubMed\]](#)
14. Zhang, Y.; Wang, S.; Wang, X.; Geng, Y. Design and control of bionic manta ray robot with flexible pectoral fin. In Proceedings of the 2018 IEEE 14th International Conference on Control and Automation (ICCA), Anchorage, AK, USA, 12–15 June 2018.
15. Bianchi, G.; Maffi, L.; Tealdi, M.; Cinquemani, S. A bioinspired cownose ray robot for seabed exploration. *Biomimetics* **2023**, *8*, 30. [\[CrossRef\]](#) [\[PubMed\]](#)
16. Hao, Y.; Cao, Y.; Cao, Y.; Huang, Q.; Pan, G. Course Control of a Manta Robot Based on Amplitude and Phase Differences. *J. Mar. Sci. Eng.* **2022**, *10*, 285. [\[CrossRef\]](#)
17. Li, Z.; Chao, X.; Hameed, I.; Li, J.; Zhao, W.; Jing, X. Biomimetic omnidirectional multi-tail underwater robot. *Mech. Syst. Signal Process.* **2022**, *173*, 109056. [\[CrossRef\]](#)
18. Fish, F.E. Advantages of aquatic animals as models for bio-inspired drones over present AUV technology. *Bioinspir. Biomim.* **2020**, *15*, 025001. [\[CrossRef\]](#)
19. Murphy, A.J.; Haroutunian, M. Using bio-inspiration to improve capabilities of underwater vehicles. In Proceedings of the 17th International Symposium on Unmanned Untethered Submersible Technology (UUST), Portsmouth, NH, USA, 21–24 August 2011; Newcastle University: Newcastle upon Tyne, UK, 2011.
20. Fish, F.E. Biomechanics and energetics in aquatic and semiaquatic mammals: Platypus to whale. *Physiol. Biochem. Zool.* **2000**, *73*, 683–698. [\[CrossRef\]](#)
21. Scaradozzi, D.; Palmieri, G.; Costa, D.; Pinelli, A. BCF swimming locomotion for autonomous underwater robots: A review and a novel solution to improve control and efficiency. *Ocean Eng.* **2017**, *130*, 437–453. [\[CrossRef\]](#)
22. Mitin, I.; Korotaev, R.; Ermolaev, A.; Mironov, V.; Lobov, S.A.; Kazantsev, V.B. Bioinspired Propulsion System for a Thunniform Robotic Fish. *Biomimetics* **2022**, *7*, 215. [\[CrossRef\]](#)
23. Zhou, J.; Si, Y.; Chen, Y. A review of subsea AUV technology. *J. Mar. Sci. Eng.* **2023**, *11*, 1119. [\[CrossRef\]](#)
24. Webb, P.W. Maneuverability—General issues. *IEEE J. Ocean. Eng.* **2004**, *29*, 547–555. [\[CrossRef\]](#)
25. Walker, J.A. Does a rigid body limit maneuverability? *J. Exp. Biol.* **2000**, *203*, 3391–3396. [\[CrossRef\]](#) [\[PubMed\]](#)
26. He, J.; Cao, Y.; Huang, Q.; Cao, Y.; Tu, C.; Pan, G. A New Type of Bionic Manta Ray Robot. In Proceedings of the Global Oceans 2020: Singapore—U.S. Gulf Coast, Biloxi, MS, USA, 5–30 October 2020. [\[CrossRef\]](#)
27. Huang, H.; Sheng, C.; Wu, J.; Wu, G.; Zhou, C.; Wang, H. Hydrodynamic analysis and motion simulation of fin and propeller driven manta ray robot. *Appl. Ocean Res.* **2021**, *108*, 102528. [\[CrossRef\]](#)
28. Raj, A.; Thakur, A. Fish-inspired robots: Design, sensing, actuation, and autonomy—A review of research. *Bioinspir. Biomim.* **2016**, *11*, 031001. [\[CrossRef\]](#) [\[PubMed\]](#)
29. Niu, C.; Zhang, L.; Bi, S.; Cai, Y. Development and depth control of a robotic fish mimicking cownose ray. In Proceedings of the 2012 IEEE International Conference on Robotics and Biomimetics (ROBIO), Guangzhou, China, 11–14 December 2012.

30. Wang, J.; Liu, Q.; Cheng, H.; Fang, B.; Zhang, J.; Hong, J. Design, fabrication and experiment of a bionic manta ray robot fish. In Proceedings of the 2022 IEEE International Conference on Robotics and Biomimetics (ROBIO), Jinghong, China, 5–9 December 2022.
31. Cai, Y.; Bi, S.; Li, G.; Hildre, H.P.; Zhang, H. From natural complexity to biomimetic simplification: The realization of bionic fish inspired by the cownose ray. *IEEE Robot. Autom. Mag.* **2018**, *26*, 27–38. [[CrossRef](#)]
32. Salazar, R.; Fuentes, V.; Abdelkefi, A. Classification of biological and bioinspired aquatic systems: A review. *Ocean Eng.* **2018**, *148*, 75–114. [[CrossRef](#)]
33. León-González, G.; Núñez-Cruz, R.S.; Antonio-Yañez, E.D.; Herrera-Vidal, J.; Canales-Gómez, G.; Rueda-Germán, C. A Unified Approach to Modeling and Simulation of Underwater Vehicle Multi-Manipulator Systems. *Machines* **2024**, *12*, 94. [[CrossRef](#)]
34. Barbalata, C. Modelling and Control of Lightweight Underwater Vehicle-Manipulator Systems. Ph.D. Thesis, Heriot-Watt University, Edinburgh, Scotland, 2017.
35. Fossen, T.I. *Handbook of Marine Craft Hydrodynamics and Motion Control*; John Wiley & Sons: Hoboken, NJ, USA, 2021.
36. Antonelli, G. *Underwater Robots: Motion and Force Control of Vehicle-Manipulator Systems (Volume 2)*; Springer: Berlin/Heidelberg, Germany, 2006.
37. Schjøberg, I.; Fossen, T. Modelling and control of underwater vehicle-manipulator systems. In Proceedings of the 3rd Conference on Marine Craft Maneuvering and Control (MCMC), Southampton, UK, 7–9 September 1994; pp. 45–57.
38. Bani Younes, A.; Turner, J.; Mortari, D.; Junkins, J. A Survey of Attitude Error Representations. In Proceedings of the AIAA/AAS Astrodynamics Specialist Conference 2012, Minneapolis, MN, USA, 13–16 August 2012. [[CrossRef](#)]
39. Jung, Y.; Cho, S.; Shim, D. A Comprehensive Flight Control Design and Experiment of a Tail-Sitter UAV. In Proceedings of the AIAA Guidance, Navigation, and Control (GNC) Conference, Chicago, IL, USA, 10–13 August 2013. [[CrossRef](#)]
40. Paschal, T.; Shintake, J.; Mintchev, S.; Floreano, D. Development of bio-inspired underwater robot with adaptive morphology capable of multiple swimming modes. In Proceedings of the 2017 IEEE/RSJ International Conference on Intelligent Robots and Systems (IROS), Vancouver, BC, Canada, 24–28 September 2017.
41. Nguyen, D.Q.; Ho, V.A. Anguilliform Swimming Performance of an Eel-Inspired Soft Robot. *Soft Robot.* **2022**, *9*, 425–439. [[CrossRef](#)]
42. Vercruyssen, T.G.A.; Henrion, S.; Müller, U.K.; van Leeuwen, J.L.; van der Helm, F.C.T. Cost of Transport of Undulating Fin Propulsion. *Biomimetics* **2023**, *8*, 214. [[CrossRef](#)]
43. Berlinger, F.; Saadat, M.; Haj-Hariri, H.; Lauder, G.V.; Nagpal, R. Fish-like three-dimensional swimming with an autonomous, multi-fin, and biomimetic robot. *Bioinspir. Biomim.* **2021**, *16*, 026018. [[CrossRef](#)]
44. Lu, B.; Zhou, C.; Wang, J.; Zhang, Z.; Tan, M. Toward Swimming Speed Optimization of a Multi-Flexible Robotic Fish With Low Cost of Transport. *IEEE Trans. Autom. Sci. Eng.* **2024**, *21*, 2804–2815. [[CrossRef](#)]
45. Hall, R.; Onal, C.D. Untethered Underwater Soft Robot with Thrust Vectoring. In Proceedings of the 2024 IEEE International Conference on Robotics and Automation (ICRA), Yokohama, Japan, 13–17 May 2024; pp. 8828–8834. [[CrossRef](#)]
46. Tong, R.; Wu, Z.; Chen, D.; Wang, J.; Du, S.; Tan, M.; Yu, J. Design and Optimization of an Untethered High-Performance Robotic Tuna. *IEEE/ASME Trans. Mechatronics* **2022**, *27*, 4132–4142. [[CrossRef](#)]
47. White, C.H.; Lauder, G.V.; Bart-Smith, H. Tunabot Flex: A tuna-inspired robot with body flexibility improves high-performance swimming. *Bioinspir. Biomim.* **2021**, *16*, 026019. [[CrossRef](#)] [[PubMed](#)]
48. Yang, S.B.; Qiu, J.; Han, X.Y. Kinematics Modeling and Experiments of Pectoral Oscillation Propulsion Robotic Fish. *J. Bionic Eng.* **2009**, *6*, 174–179. [[CrossRef](#)]
49. Cao, Y.; Lu, Y.; Cai, Y.; Bi, S.; Pan, G. CPG-fuzzy-based control of a cownose-ray-like fish robot. *Ind. Robot. Int. J. Robot. Res. Appl.* **2019**, *46*, 779–791. [[CrossRef](#)]
50. Ma, H.; Cai, Y.; Wang, Y.; Bi, S.; Gong, Z. A biomimetic cownose ray robot fish with oscillating and chordwise twisting flexible pectoral fins. *Ind. Robot. Int. J.* **2015**, *42*, 214–221. [[CrossRef](#)]
51. Ji, Y.; Wei, Y.; Liu, J.; An, D. Design and Realization of a Novel Hybrid-Drive Robotic Fish for Aquaculture Water Quality Monitoring. *J. Bionic Eng.* **2022**, *20*, 543–557. [[CrossRef](#)]
52. Zhang, L.; Niu, C.; Bi, S.; Cai, Y. Kinematic model analysis and design optimization of a bionic pectoral fins. In Proceedings of the 2013 IEEE International Conference on Robotics and Biomimetics (ROBIO), Shenzhen, China, 12–14 December 2013; Volume 32, pp. 2219–2224. [[CrossRef](#)]
53. Niu, C.; Zhang, L.; Bi, S.; Cai, Y. Mechanical design and implementation of a bio-inspired robotic fish with flapping foils. In Proceedings of the 2013 IEEE International Conference on Robotics and Biomimetics (ROBIO), Shenzhen, China, 12–14 December 2013; Volume 204, pp. 2291–2296. [[CrossRef](#)]
54. Chen, L.; Bi, S.; Cai, Y.; Cao, Y.; Pan, G. Design and Experimental Research on a Bionic Robot Fish with Tri-Dimensional Soft Pectoral Fins Inspired by Cownose Ray. *J. Mar. Sci. Eng.* **2022**, *10*, 537. [[CrossRef](#)]

Disclaimer/Publisher’s Note: The statements, opinions and data contained in all publications are solely those of the individual author(s) and contributor(s) and not of MDPI and/or the editor(s). MDPI and/or the editor(s) disclaim responsibility for any injury to people or property resulting from any ideas, methods, instructions or products referred to in the content.